Biomechanics and Modeling in Mechanobiology manuscript No.
(will be inserted by the editor)

Application of the multiscale FEM to the modeling of cancellous bone

Sandra Ilic · **Klaus Hackl** · **Robert Gilbert**

Received: date / Accepted: date

Abstract This paper considers the application of multiscale finite element method (FEM) to the modeling of cancellous bone as an alternative for Biot's model, whereby the main intention is to decrease the extent of the necessary laboratory tests. At the beginning the paper gives a brief explanation of the multiscale concept and thereafter focuses on the modeling of the representative volume element (RVE) and on the calculation of the effective material parameters including an analysis of their change with respect to increasing porosity. The latter part of the paper concentrates on the macroscopic calculations, which is illustrated by the simulation of ultrasonic testing and a study of the attenuation dependency on material parameters and excitation frequency. The results endorse conclusions drawn from the experiments: increasing excitation frequency and material density cause increasing attenuation.

Keywords Multiscale FEM · Attenuation · Cancellous bone · Homogenization

1 Introduction

In recent times, the investigation of the effective properties of cancellous bone has been especially intensive as it may lead to the early detecting of osteoporosis. This pathological process manifests itself through increasing bone resorption and decreasing bone production. In its late stage, even entire walls of the solid bone frame disappear leading to abrupt decrease of material strength. The laboratory measurements show that during the process porosity increases from 72% up to 95% causing the density to change from 1200 to 1000 kg/m^3.

For the investigation of cancellous bone different approaches are developed, some of them being of experimental character, the other ones focusing on developing a convenient mathematical or mechanical model. Among the experimental methods the dual X-ray absorptiometry (DXA) and the quantitative ultrasonic (QUS) technique are the ones mostly used, but the latter has a few important advantages: while the DXA is convenient only for investigation of bone mineralogy density (BMD), the QUS technique yields data on the speed of sound (SOS) and broadband ultrasonic attenuation (BUA), two parameters strongly related to the microstructure of trabecular bone and significantly influencing its strength (Hosokawa and Otani, 1997; Zysset et al, 1999; Barkmann et al, 2000a; Bossy et al, 2004a; Laugier et al, 1994a). Moreover, in contrast to X-ray technology, ultrasound does not ionize the tissue and its implementation is relatively inexpensive.

Among the analytic solutions, those based on Biot's theory (Biot, 1956a,b) are certainly established as the leading ones. The shortcoming of these methods is its dependence on many material parameters which have to be determined experimentally. An analytical approach to the investigation of these parameters and especially of the accuracy up to which they can be determined, is presented in works of Buchanan et al (2004) and Buchanan and Gilbert (2006).

Finally, the rush development of computer technology gave a new aspect to the bone modeling where the application of numerical solvers plays an important role. Here

S. Ilic
Institute of Mechanics,
Ruhr-University Bochum,
D-44780 Bochum, Germany
E-mail: sandra.ilic@rub.de

K. Hackl
Institute of Mechanics,
Ruhr-University Bochum,
D-44780 Bochum, Germany

R. Gilbert
Department of Mathematical Sciences,
University of Delaware,
Newark DE, USA

also two groups of methods deserve to be mentioned: the finite difference time domain (FDTD) technique and the finite element method (FEM). The FDTD method was first applied in biomechanics by Luo et al (1999), and since then has gained in importance. For example, Hosokawa (2006) used this method to simulate biphasic materials according to the purely viscoelastic theory and according to Biot's theory for porous media, while the most recent works in this field consider 3D simulations (Bossy et al, 2005, 2004; Haïat et al, 2007). Simulations based on a true reproduction of microstructure geometry are also an actual topic within the scope of the FEM application. Here the accent is especially put on the digital image based meshing process (Bayraktar et al, 2004; Hollister and Kikuchi, 1994; Niebur et al, 2000; Rietbergen et al, 1996).

This paper also reports on the results obtained by using the FEM or more precisely, the multiscale FEM (Ilic and Hackl, 2004, 2007; Ilic, 2008; Miehe et al, 2002; Schröder, 2000; Pahr and Zysset, 2008). The method is applied in the context of sound excitation (Hackl, 1998; Gilbert et al, 1998) where three ranges are to be distinguished: low frequencies (100-500 kHz), the resonance frequency (about 500 KHz), and high frequencies (0.5-2MHz). The lower frequencies are convenient for a parameter analysis while the higher ones, especially in the range of 1-2MHz, are used for investigation of the attenuation effects. In contrast to the digital image technique where the intention is to map the realistic structure to the FE model, this work investigates a relatively simple geometry whose analysis yields effective material properties. Indeed, bearing in mind the real physical microstructure, it can be expected that local differences in trabeculaemesh can be neglected, and that it can be substituted by the mesh of periodically repeated representative cells. In the model presented here such a cell consists of a solid frame and fluid marrow, both simulated as viscoelastic materials with the energy absorption influencing the macroscopic attenuation. Due to its simplicity, the assumed concept seems to be convenient for an iterative procedure typical for inverse problems where the optimal geometrical parameters of the microstructure are determined.

Within the paper, the applied procedure and obtained results are presented as follows: Chapter 2 considers the multiscale FEM which is a method resulting from the coupling of homogenization theory with FEM. Particular attention is given to derivation of boundary conditions at the microlevel.

Chapter 3 focuses on calculations at microscale. It first explains the concept of the RVE additionally giving some further details about the modeling of the solid and fluid phase. The standard as well as the extended formulation of the shell element and 8-node cubic element are described. The extension concerns modeling in the complex domain where the imaginary part is responsible for the internal material friction. Furthermore effective elasticity tensors and parameters are studied. Attention is drawn to their change with respect to increasing porosity which is simulated changing the geometry of the RVE.

Chapter 4 concentrates on macroscale simulation where the ultrasonic attenuation test is used for illustration. In this chapter, the details about the model and results of a standard test are described. The final simulations concern the calculation of the attenuation coefficients and an analysis of their dependence on material properties and excitation frequency. The paper closes with a short overview and outlook.

2 Concept of the multiscale FEM

Multiscale FEM belongs to the group of homogenization methods so that it is applicable only in the case of statistically uniform materials (Mura, 1993; Nemat-Nasser and Hori, 1993; Torquato, 2002; Willis, 1981, 1982; Zohdi and Wriggers, 2005). For this kind of materials, it is typical that they possess a representative volume element (RVE) whose analysis yields the effective material parameters, but the limiting condition is that the ratio of the characteristic lengths of RVE and the simulated body has to tend to zero. This is from where the usual terminology macro- and microscale is derived. As both scales are analyzed simultaneously, the standard notation distinguishes between quantities related to the different scales by introducing an overbar symbol. Thus position vector, displacements vector, strain tensor, stress tensor, and potential respectively are denoted by

$\bar{\mathbf{x}},\ \bar{\mathbf{u}},\ \bar{\varepsilon},\ \bar{\sigma},\ \bar{\psi}=\bar{\psi}(\bar{\varepsilon},\bar{\mathbf{x}})$ at the macrocontinuum,

$\mathbf{x},\ \mathbf{u},\ \varepsilon,\ \sigma,\ \psi=\psi(\varepsilon,\mathbf{x})$ at the microcontinuum.

The method is based on the principle of volume averaging, leading to the definition of the macrostress tensor in the form

$$\bar{\sigma}=\frac{1}{V}\int_{\mathscr{B}}\sigma dV$$

where the integration is carried out over the RVE $\mathscr{B}$, with the volume V. Note that within the scope of bone modeling, consideration is given to the theory of small deformations.

The well-posedness of the problem on the microscale also requires the equality of macrowork with the volume average of microwork

$$\bar{\sigma}:\bar{\varepsilon}=\frac{1}{V}\int_{\mathscr{B}}\sigma:\varepsilon\ dV \tag{1}$$

which is known as Hill-Mandel macrohomogeneity condition (Hill, 1963, 1972). Expression (1) is satisfied by three types of boundary conditions at the microlevel: static, kinematic, and periodic ones. It is also worth mentioning that within the scope of cancellous bone modeling and especially in approaches where the accent is put on a realistic representation of geometry (Pahr and Zysset, 2008), the consideration of a sample smaller than the present RVE is often

needed. Such an analysis yields ”apparent” instead of effective material parameters and apart from the static, kinematic and periodic boundary conditions also the mixed boundary conditions guarantee that Hill's condition is fulfilled (Hazanov and Amieur, 1995; Ostoja-Starzewski, 2006). As we assume in our model that without loss of generality the microstructure consists of periodically repeated RVE's, we will work in the following analysis exclusively with periodic bou ndary conditions. In this case the microdeformation, is assumed to be dependent on the macrostrain tensor $\bar{\varepsilon}$ and on the microfluctuations $\tilde{\mathbf{u}}$

$$\mathbf{u} = \bar{\varepsilon}\mathbf{x} + \tilde{\mathbf{u}}. \tag{2}$$

Now microfluctuations have to be periodic and traction antiperiodic on the periodic boundary of the RVE

$$\begin{aligned} \tilde{\mathbf{u}}^+ &= \tilde{\mathbf{u}}^-, \\ \mathbf{t}^+ &= -\mathbf{t}^- \end{aligned}$$

and the additive decomposition is characteristic for the microstrain tensor

$$\varepsilon = \bar{\varepsilon} + \tilde{\varepsilon}, \qquad \tilde{\varepsilon} = \frac{1}{2}(\nabla\tilde{\mathbf{u}} + \tilde{\mathbf{u}}\nabla) = \nabla^{\mathrm{s}}\tilde{\mathbf{u}}. \tag{3}$$

Such a decomposition permits to split the problem of simulation of a heterogeneous body into two parts, each consisting of one boundary value problem (BVP). The first BVP relates to the simulation of the homogenized macroscopic body and the second one to the analysis of the RVE.

For solving these two BVPs, any standard method can be applied and FEM is chosen here for this purpose. Moreover, using the described theory and standard program FEAP (Zienkiewicz and Taylor, 2000), a new multiscale FE program is written. Its main difference in comparison with a standard FE program code is that calculations at the microlevel replace the missing effective constitutive law at the macroscale (Fig. 1).

The simplified flow chart (Fig. 1) shows that macroscale calculations provide the macrostrain tensor $\bar{\varepsilon}$ which has to be understood as a priori given at the microlevel. Solution of the BVP at this level results in distributions of the microfluctuations $\tilde{\mathbf{u}}$ and of the microstresses σ whose volume average represents the sought counterpart on the macrolevel $\bar{\sigma}$. The calculations at this level also supply the elasticity tensor $\bar{C}$. In contrast to the case of finite deformations, this tensor has to be calculated only once as it is independent from the deformation state.

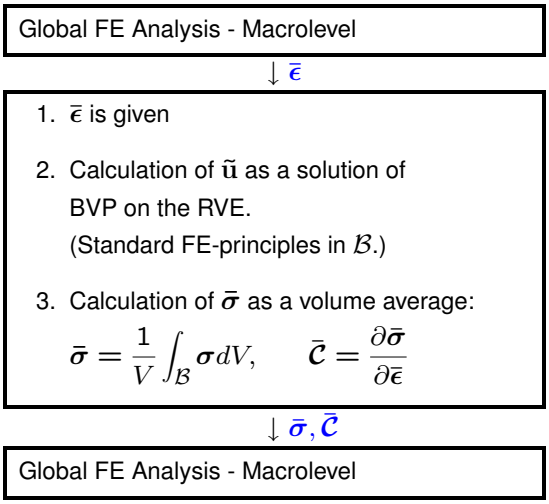

Fig. 1 Connection of scales in the program code.

3 Microscale: Modeling of the RVE and calculation of the effective material properties

3.1 Modeling of the RVE for cancellous bone

Due to the complex geometry of cancellous bone, different types of the RVE can be proposed for its modeling. Moreover, it is well known that the bone structure changes dependent on many factors and that the deterioration of trabecular bone is characterized by a conversion from bone plates to bone rods. Consequently the terms ”rod-like” and ”plate-like” are frequently used for a subjective classification of cancellous bone. For an objective quantification a morphometric parameter called structure model index (SMI) is introduced by Hildebrand and Rüegsegger (1997). This index shows the amount of plates and rods composing the structure, and for an ideal plate and rod structure the SMI value is 0 and 3 respectively. In our model we treat the solid frame as a system of thin walls whose thickness and width can be varied. In limit cases such an RVE can contain complete solid facets or thin columns in its edges. The RVE is assumed to have a cubic form with the side length *a*. The other parameters that are needed to completely determine the RVE, are thickness of the wall *d* and width of the wall *b*. Figure 2 shows an example of the real microstructure of cancellous bone affected by osteoporosis, and a proposal for the corresponding RVE. In the part of figure that shows the real structure of the bone, it can be seen that most of the solid walls are resorbed and only the edge columns remain.

To calculate the effective material parameters, a dynamic analysis of the proposed RVE is necessary, and periodic excitation is preferable because of its simplicity. In such a case, the load and induced deformations are harmonic functions in time

$$\mathbf{p}(\mathbf{x},t) = \mathbf{p}(\mathbf{x})e^{i\omega t}, \qquad \mathbf{u}(\mathbf{x},t) = \mathbf{u}(\mathbf{x})e^{i\omega t}, \tag{4}$$

where $\mathbf{p}(\mathbf{x})$ and $\mathbf{u}(\mathbf{x})$ may be complex-valued, ω is the frequency of excitation and *i* represents the imaginary unit. The application of (4) yields the simplified form of the equation

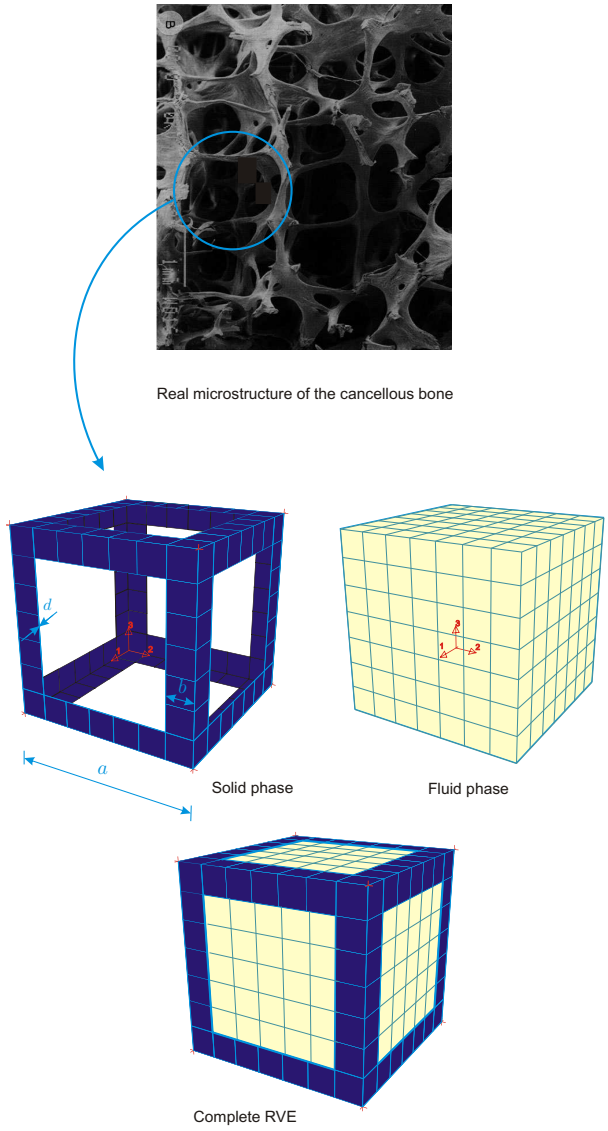

Fig. 2 Real bone microstructure and corresponding RVE.

of motion

$$\rho(\mathbf{x})\ddot{\mathbf{u}}(\mathbf{x},t) - \nabla\cdot\sigma(\mathbf{x},t) = \rho(\mathbf{x})\mathbf{b}(\mathbf{x},t)$$
$$\downarrow$$
$$-\omega^2\rho(\mathbf{x})\mathbf{u}(\mathbf{x}) - \nabla\cdot\sigma(\mathbf{x}) = \rho(\mathbf{x})\mathbf{b}(\mathbf{x})$$

depending on density $\rho(\mathbf{x})$ and body forces $\mathbf{b}(\mathbf{x})$. To describe the problem completely, the constitutive laws of the fluid and solid phase still need to be stated precisely. Regarding the bone material, a linear analysis is typical so that for the solid part a linear relation between stresses and strains (6) and for the marrow the constitutive law of barotropic fluids (8) are assumed. The state of deformations in the solid part Ω_s can now be described by the system

$$-\omega^2\rho_\mathrm{s}\mathbf{u} - \nabla\cdot\sigma_\mathrm{s} = \rho_\mathrm{s}\mathbf{b}(\mathbf{x}), \tag{5}$$

$$\sigma_\mathrm{s} = \boldsymbol{C} : \varepsilon \tag{6}$$

and in the fluid part Ω_f, by:

$$-\omega^2\rho_\mathrm{f}\mathbf{u} - \nabla\cdot\sigma_\mathrm{f} = \rho_\mathrm{f}\mathbf{b}(\mathbf{x}), \tag{7}$$

$$\sigma_\mathrm{f} = c^2\rho_\mathrm{f}\nabla\cdot\mathbf{u}\,\mathbf{I} + 2i\omega\eta\,\varepsilon + i\omega\xi\,\nabla\cdot\mathbf{u}\,\mathbf{I}. \tag{8}$$

Here $\boldsymbol{C}$ is the elasticity tensor of the solid phase, $\mathbf{I}$ the identity tensor, c the sound velocity of the marrow so that $c = \sqrt{K/\rho_\mathrm{f}}$, K is the bulk modulus, η and ξ are the viscosity coefficients. The indices s and f are used to distinguish the phases. Furthermore, the coupling condition between the phases requires that there is no deformation jump on the interface of phases

$$\mathbf{u}_\mathrm{s} = \mathbf{u}_\mathrm{f} \quad \text{on} \quad \Gamma = \Omega_\mathrm{s} \cap \Omega_\mathrm{f}. \tag{9}$$

Recall that all the expressions (5)-(9) are defined in the complex domain. The material parameters of the solid phase, bulk modulus K_s and shear modulus μ_s are also complex-valued an they can be written in the form

$$K_\mathrm{s} = K_\mathrm{s}^\mathrm{R} + iK_\mathrm{s}^\mathrm{I}, \qquad \mu_\mathrm{s} = \mu_\mathrm{s}^\mathrm{R} + i\mu_\mathrm{s}^\mathrm{I} \tag{10}$$

where the imaginary parts are related to the real ones according to

$$K_\mathrm{s}^\mathrm{I} = \frac{\delta}{\pi}K_\mathrm{s}^\mathrm{R}, \qquad \mu_\mathrm{s}^\mathrm{I} = \frac{\delta}{\pi}\mu_\mathrm{s}^\mathrm{R}, \tag{11}$$

and δ denotes the logarithmic decrement amounting to 0.1 for underwater acoustics (Buchanan et al, 2002, 2004; Fang et al, 2007). Remaining material parameters appearing in the constitutive laws defined above, are listed in Table 1.

Table 1 Parameters for cancellous bone due to Williams and Johnson (1989).

Parameter	**Sym.**	**Value**	**Unity**
Pore fluid density	ρ_f	950	kg m^{-3}
Fluid bulk modulus	K_f	2.00×10^9	Pa
Pore fluid viscosity	η	1.5	Ns m^{-2}
Frame material density	ρ_s	1960	kg m^{-3}
Bulk modulus of the solid phase (real)	K_s^R	2.04×10^{10}	Pa
Shear modulus of the solid phase (real)	$\mu_\mathrm{s}^\mathrm{R}$	0.833×10^{10}	Pa
Young's modulus of the solid phase (real)	E_s^R	2.2×10^{10}	Pa
Poisson's ratio	ν	0.32	-

3.2 Modeling of the solid phase

Due to the geometric properties, we are going to model the solid phase by using the shell elements (see i.e. Hackl (1997)), but as the shell elements already implemented in the program FEAP (Zienkiewicz and Taylor, 2000) are not applicable for simulations in the complex domain, further adaption has been necessary. In particular we focused on the extension of an element convenient for simulation of flat and shallow shells. The formulation of this element is based on the superposition of the linear theory for a plate loaded in its plane and a plate loaded by bending, whose potentials are

$$\Pi_{\mathrm{p}}^{\mathrm{e}} = \Pi_{\mathrm{p}}^{\mathrm{e,int}} + \Pi_{\mathrm{p}}^{\mathrm{e,ext}} = \frac{1}{2}\int_{\mathscr{A}^{\mathrm{e}}} \mathbf{u}^{\mathrm{T}}\cdot\mathbf{L}_{\mathrm{p}}^{\mathrm{T}}\cdot\boldsymbol{C}_{\mathrm{p}}\cdot\mathbf{L}_{\mathrm{p}}\cdot\mathbf{u}\,da + \Pi_{\mathrm{p}}^{\mathrm{e,ext}}, \tag{12}$$

$$\Pi_{\mathrm{b}}^{\mathrm{e}} = \Pi_{\mathrm{b}}^{\mathrm{e,int}} + \Pi_{\mathrm{b}}^{\mathrm{e,ext}} = \frac{1}{2}\int_{\mathscr{A}^{\mathrm{e}}} \theta^{\mathrm{T}}\cdot\mathbf{L}_{\mathrm{b}}^{\mathrm{T}}\cdot\boldsymbol{C}_{\mathrm{b}}\cdot\mathbf{L}_{\mathrm{b}}\cdot\theta\,da + \Pi_{\mathrm{b}}^{\mathrm{e,ext}}. \tag{13}$$

Hereafter subscript p is taken to denote the plate loaded in its plane and subscript b for the bending of plate, e indicates that a single element is considered. $\mathbf{L}_{\mathrm{p}}$ and $\mathbf{L}_{\mathrm{b}}$ are linear operators and $\boldsymbol{C}_{\mathrm{p}}$ and $\boldsymbol{C}_{\mathrm{b}}$ material tensors whose precise definition can be found in the literature (Batoz and Tahar, 1982; Ilic, 2008; Taylor, 1998; Wanji and Cheung, 1997; Zienkiewicz and Taylor, 2000). The integration is carried out over the middle area of the element $\mathscr{A}^{\mathrm{e}}$. As expression (12) depends on the displacements $\mathbf{u}_{\mathrm{p}} = \{u\ v\}^{\mathrm{T}}$ and (13) on the rotations $\theta = \{\theta_x\ \theta_y\}^{\mathrm{T}}$, a FE approximation

$$\mathbf{u}^{\mathrm{m}} = \mathbf{N}^{\mathrm{m}}\cdot\hat{\mathbf{a}}^{\mathrm{me}}, \tag{14}$$

$$\mathbf{u}^{\mathrm{m}} = \left\{ u\ v\ \theta_x\ \theta_y \right\}^{\mathrm{T}}, \quad \hat{\mathbf{a}}_i^{\mathrm{m}} = \left\{ \hat{u}_i\ \hat{v}_i\ \hat{\theta}_{zi}\ \hat{w}_i\ \hat{\theta}_{xi}\ \hat{\theta}_{yi} \right\}^{\mathrm{T}} \tag{15}$$

leads after substitution into the first variation of (12) and (13) to the weak form of the problem

$$\begin{aligned}
&\delta\Pi^{\mathrm{e}} = \\
&= (\delta\hat{\mathbf{a}}^{\mathrm{me}})^{\mathrm{T}}\cdot\left(\int_{\mathscr{A}^{\mathrm{e}}} (\mathbf{N}^{\mathrm{m}})^{\mathrm{T}}\cdot\mathbf{L}^{\mathrm{T}}\cdot\boldsymbol{C}\cdot\mathbf{L}\cdot\mathbf{N}^{\mathrm{m}}\,da\right)\cdot\hat{\mathbf{a}}^{\mathrm{me}} + \delta\Pi^{\mathrm{e,ext}} \\
&= (\delta\hat{\mathbf{a}}^{\mathrm{me}})^{\mathrm{T}}\cdot\left(\int_{\mathscr{A}^{\mathrm{e}}} (\mathbf{B}^{\mathrm{m}})^{\mathrm{T}}\cdot\boldsymbol{C}\cdot\mathbf{B}^{\mathrm{m}}\,da\right)\cdot\hat{\mathbf{a}}^{\mathrm{me}} + \delta\Pi^{\mathrm{e,ext}}.
\end{aligned} \tag{16}$$

In expressions (14) and (15), $\mathbf{N}^{\mathrm{m}}$ represents the matrix of the shape functions, and superscript m indicates that a modified approximation is used ($\hat{\theta}_{zi}$ and $\hat{w}_i$ are used in the approximation of the vector $\mathbf{u}$), the symbol $\hat{\mathbf{a}}^{\mathrm{me}}$ relates to the vector of the element DOFs and $\hat{\mathbf{a}}_i^{\mathrm{m}}$ to the vector of the nodal DOFs. The matrices appearing in (16) are composed as follows

$$\mathbf{L} = \begin{bmatrix} \mathbf{L}_{\mathrm{p}} & 0 \\ 0 & \mathbf{L}_{\mathrm{b}} \end{bmatrix}, \qquad \mathbf{B}^{\mathrm{m}} = \mathbf{L}\cdot\mathbf{N}^{\mathrm{m}}, \qquad \boldsymbol{C} = \begin{bmatrix} \boldsymbol{C}_{\mathrm{p}} & 0 \\ 0 & \boldsymbol{C}_{\mathrm{b}} \end{bmatrix} \tag{17}$$

Note that the described element (Taylor, 1998; Zienkiewicz and Taylor, 2000) is also adapted to structures with small curvature by introducing correction factors in which case the formulation, in contrast to (17), becomes coupled. The weak form of the problem (16) finally results in the discretized equilibrium equation of an element dependent on the stiffness matrix $\mathbf{K}^{\mathrm{e}}$ and the vector of nodal forces $\mathbf{f}^{\mathrm{e}}$

$$\mathbf{K}^{\mathrm{e}}\cdot\hat{\mathbf{a}}^{\mathrm{me}} = \mathbf{f}^{\mathrm{e}}. \tag{18}$$

Furthermore, the application of the element in the dynamic case requires the minimization of the Lagrangian

$$\delta\int_t (E_k - \Pi)\,dt = 0 \tag{19}$$

where integration of the time t is considered, Π is the total potential including (12) and (13), and E_k represents the kinetic energy

$$E_{\mathrm{k}} = \frac{1}{2}\int_{\Omega} \rho\,\dot{\mathbf{u}}^{T}\cdot\dot{\mathbf{u}}\,dv \tag{20}$$

with the first variation in the form

$$\delta\int_t E_{\mathrm{k}}(\dot{\mathbf{u}})\,dt = \omega^2\int_t\int_{\Omega} \rho\,\delta\mathbf{u}^{T}\cdot\mathbf{u}\,dv\,dt. \tag{21}$$

As this expression only depends on the acceleration and indirectly on the displacements, a simplified FE approximation is introduced here:

$$\mathbf{u} = \mathbf{N}\cdot\hat{\mathbf{a}}^{\mathrm{me}}, \tag{22}$$

$$\mathbf{u} = \left\{ u\ v\ w \right\}^{\mathrm{T}}, \qquad \hat{\mathbf{a}}_i^{\mathrm{m}} = \left\{ \hat{u}_i\ \hat{v}_i\ \hat{\theta}_{zi}\ \hat{w}_i\ \hat{\theta}_{xi}\ \hat{\theta}_{yi} \right\}^{\mathrm{T}}. \tag{23}$$

Substitution of (22) in (21) and using (18) and (19) now leads to the discretized equation of motion including the mass matrix $\mathbf{M}^{\mathrm{e}}$

$$\left(-\omega^2\mathbf{M}^{\mathrm{e}} + \mathbf{K}^{\mathrm{e}}\right)\cdot\hat{\mathbf{a}}^{\mathrm{me}} = \mathbf{f}^{\mathrm{e}}, \qquad \mathbf{M}^{\mathrm{e}} = \int_{\Omega^{\mathrm{e}}} \rho\,\mathbf{N}^{\mathrm{T}}\cdot\mathbf{N}dv \tag{24}$$

where the integral over the time could be left out due to the periodicity of the load and deformations.

The final extension from the real to the complex domain includes steps similar to those previously described. As here the displacements and the rotations poses the imaginary counterparts, the following approximations have to be used instead of (14) and (22)

$$\mathbf{u}_{\mathrm{c}}^{\mathrm{m}} = \left\{ (\mathbf{u}^{\mathrm{mR}})^{\mathrm{T}} \quad i(\mathbf{u}^{\mathrm{mI}})^{\mathrm{T}} \right\}^{\mathrm{T}}, \quad \mathbf{u}_{\mathrm{c}} = \left\{ (\mathbf{u}^{\mathrm{R}})^{\mathrm{T}} \quad i(\mathbf{u}^{\mathrm{I}})^{\mathrm{T}} \right\}^{\mathrm{T}},$$

$$\hat{\mathbf{a}}_{\mathrm{c}}^{\mathrm{me}} = \left\{ (\hat{\mathbf{a}}^{\mathrm{eR}})^{\mathrm{T}} \quad i(\hat{\mathbf{a}}^{\mathrm{eI}})^{\mathrm{T}} \right\}^{\mathrm{T}},$$

$$\mathbf{u}_{\mathrm{c}}^{\mathrm{m}} = \mathbf{N}_{\mathrm{c}}^{\mathrm{m}}\cdot\hat{\mathbf{a}}_{\mathrm{c}}^{\mathrm{me}}, \qquad \mathbf{N}_{\mathrm{c}}^{\mathrm{m}} = \begin{bmatrix} \mathbf{N}^{\mathrm{m}} & 0 \\ 0 & \mathbf{N}^{\mathrm{m}} \end{bmatrix}, \tag{25}$$

$$\mathbf{u}_{\mathrm{c}} = \mathbf{N}_{\mathrm{c}}\cdot\hat{\mathbf{a}}_{\mathrm{c}}^{\mathrm{me}}, \qquad \mathbf{N}_{\mathrm{c}} = \begin{bmatrix} \mathbf{N} & 0 \\ 0 & \mathbf{N} \end{bmatrix}. \tag{26}$$

Here the real and imaginary DOFs of an element are grouped separately, which is convenient for further derivations. The index c denotes the complex quantities. Due to the complex material parameters (11) the elasticity tensor also has complex form with the real and imaginary submatrices dependent on the real and imaginary part of Young's modulus and Poisson's number

$$\boldsymbol{C}_{\mathrm{c}} = \begin{bmatrix} \boldsymbol{C}^{\mathrm{R}} & i\boldsymbol{C}^{\mathrm{I}} \\ i\boldsymbol{C}^{\mathrm{I}} & \boldsymbol{C}^{\mathrm{R}} \end{bmatrix}, \quad \boldsymbol{C}^{\mathrm{R}} = \boldsymbol{C}(E^{\mathrm{R}}, \nu), \quad \boldsymbol{C}^{\mathrm{I}} = \boldsymbol{C}(E^{\mathrm{I}}, \nu). \tag{27}$$

Equation (11) and standard relations between material parameters may be used to show that $E^{\mathrm{I}} = \frac{\delta}{\pi} E^{\mathrm{R}}$ and that the imaginary part of Poisson's ratio (for this particular case) is equal to zero. The implementation of (25)-(27) into complex counterparts of (16) and (21) now gives the complex form of the equation of motion

$$\left(-\omega^2 \mathbf{M}_{\mathrm{c}}^{\mathrm{e}} + \mathbf{K}_{\mathrm{c}}^{\mathrm{e}}\right) \cdot \hat{\mathbf{a}}_{\mathrm{c}}^{\mathrm{m\,e}} = \mathbf{f}_{\mathrm{c}}^{\mathrm{e}} \tag{28}$$

dependent on the following quantities

$$\mathbf{M}_{\mathrm{c}}^{\mathrm{e}} = \int_{\Omega^{\mathrm{e}}} \rho \mathbf{N}_{\mathrm{c}}^{\mathrm{T}} \cdot \mathbf{N}_{\mathrm{c}}\, dv = \begin{bmatrix} \mathbf{M}^{\mathrm{e}} & 0 \\ 0 & \mathbf{M}^{\mathrm{e}} \end{bmatrix}, \tag{29}$$

$$\mathbf{K}_{\mathrm{c}}^{\mathrm{e}} = \int_{\mathscr{A}^{\mathrm{e}}} (\mathbf{B}_{\mathrm{c}}^{\mathrm{m}})^{T} \cdot \boldsymbol{C} \cdot \mathbf{B}_{\mathrm{c}}^{\mathrm{m}}\, da = \begin{bmatrix} \mathbf{K}^{\mathrm{eR}} & i\mathbf{K}^{\mathrm{eI}} \\ i\mathbf{K}^{\mathrm{eI}} & \mathbf{K}^{\mathrm{eR}} \end{bmatrix}, \tag{30}$$

$$\mathbf{B}_{\mathrm{c}}^{\mathrm{m}} = \mathbf{L}_{\mathrm{c}} \cdot \mathbf{N}_{\mathrm{c}}^{\mathrm{m}} = \begin{bmatrix} \mathbf{B}^{\mathrm{m}} & 0 \\ 0 & \mathbf{B}^{\mathrm{m}} \end{bmatrix}, \qquad \mathbf{L}_{\mathrm{c}} = \begin{bmatrix} \mathbf{L} & 0 \\ 0 & \mathbf{L} \end{bmatrix}. \tag{31}$$

Note that in the present model the imaginary parts of the elasticity tensor are used to introduce the attenuation effects, while, in the engineering practice, Rayleigh damping is applied for it. According to this approach an additive decomposition of the damping matrix into two parts proportional to the mass matrix and stiffness matrix is assumed (Bathe, 1996; Zienkiewicz and Taylor, 2000).

3.3 Modeling of the fluid phase

An extension to the complex domain is also necessary for the 8-node cubic element chosen to simulate the marrow part. As in this case the derivation procedure is much simpler, it can be started directly using the complex form of the potential characteristic for this element

$$L = \frac{1}{2} \int_{\Omega} \rho\, \dot{\mathbf{u}}_{\mathrm{c}}^{\mathrm{T}} \cdot \dot{\mathbf{u}}_{\mathrm{c}}\, dv - \frac{1}{2} \int_{\Omega} \boldsymbol{\varepsilon}_{\mathrm{c}} \cdot \boldsymbol{C}_{\mathrm{c}} \cdot \boldsymbol{\varepsilon}_{\mathrm{c}}\, dv - \Pi^{\mathrm{ext}}. \tag{32}$$

Here the vector of the complex displacements

$$\begin{aligned} \mathbf{u}_{\mathrm{c}} &= \left\{ (\mathbf{u}^{\mathrm{R}})^{\mathrm{T}} \;\; i(\mathbf{u}^{\mathrm{I}})^{\mathrm{T}} \right\}^{\mathrm{T}} \\ &= \left\{ u^{\mathrm{R}} \quad v^{\mathrm{R}} \quad w^{\mathrm{R}} \quad iu^{\mathrm{I}} \quad iv^{\mathrm{I}} \quad iw^{\mathrm{I}} \right\}^{\mathrm{T}} \end{aligned} \tag{33}$$

has to be approximated in the following way:

$$\mathbf{u}_{\mathrm{c}} = \mathbf{N}_{\mathrm{c}} \cdot \hat{\mathbf{a}}_{\mathrm{c}}^{\mathrm{e}}, \tag{34}$$

$$\hat{\mathbf{a}}_{\mathrm{c}}^{\mathrm{e}} = \left\{ (\hat{\mathbf{a}}^{\mathrm{eR}})^{\mathrm{T}} \quad i(\hat{\mathbf{a}}^{\mathrm{eI}})^{\mathrm{T}} \right\}^{\mathrm{T}}, \quad \mathbf{N}_{\mathrm{c}} = \begin{bmatrix} \mathbf{N} & 0 \\ 0 & \mathbf{N} \end{bmatrix} \tag{35}$$

$$\hat{\mathbf{a}}_i^{\mathrm{R}} = \left\{ \hat{u}^{\mathrm{R}} \quad \hat{v}^{\mathrm{R}} \quad \hat{w}^{\mathrm{R}} \right\}^{\mathrm{T}}, \qquad \hat{\mathbf{a}}_i^{\mathrm{I}} = \left\{ \hat{u}^{\mathrm{I}} \quad \hat{v}^{\mathrm{I}} \quad \hat{w}^{\mathrm{I}} \right\}^{\mathrm{T}} \tag{36}$$

and $\mathbf{N}$ represents the matrix consisting of the shape functions typical for the standard 8-node element of the program FEAP (Bathe, 1996; Zienkiewicz and Taylor, 2000). By using approximation (34) and the complex elasticity tensor based on (8), the variation of (32) becomes

$$-\omega^2 (\delta \hat{\mathbf{a}}_{\mathrm{c}}^{\mathrm{e}})^{\mathrm{T}} \cdot \left(\int_{\Omega^{\mathrm{e}}} \rho \mathbf{N}_{\mathrm{c}}^{\mathrm{T}} \cdot \mathbf{N}_{\mathrm{c}}\, dv \right) \cdot \hat{\mathbf{a}}_{\mathrm{c}}^{\mathrm{e}} +$$

$$(\delta \hat{\mathbf{a}}_{\mathrm{c}}^{\mathrm{e}})^{\mathrm{T}} \cdot \left(\int_{\Omega^{\mathrm{e}}} \mathbf{N}_{\mathrm{c}}^{\mathrm{T}} \cdot \mathbf{L}_{\mathrm{c}}^{\mathrm{T}} \cdot \boldsymbol{C}_{\mathrm{c}} \cdot \mathbf{L}_{\mathrm{c}} \cdot \mathbf{N}_{\mathrm{c}}\, dv \right) \cdot \hat{\mathbf{a}}_{\mathrm{c}}^{\mathrm{e}} + \delta \Pi^{\mathrm{e,ext}} = 0$$

yielding the equation of motion

$$\left(-\omega^2 \mathbf{M}_{\mathrm{c}}^{\mathrm{e}} + \mathbf{K}_{\mathrm{c}}^{\mathrm{e}}\right) \cdot \hat{\mathbf{a}}_{\mathrm{c}}^{\mathrm{m\,e}} = \mathbf{f}_{\mathrm{c}}^{\mathrm{e}} \tag{37}$$

Although the same notation is used as in the case of shell element (28), all the quantities appearing here are defined in a different manner, corresponding to the solid element.

3.4 Summary of the equations defining the BVP on the microlevel

Let us for convenience summarize the description of the RVE

$$(-\omega^2 \mathbf{M}_{\mathrm{s}} + \mathbf{K}_{\mathrm{s}}) \cdot \tilde{\mathbf{a}}_{\mathrm{s}} = \mathbf{f}_{\mathrm{s}}(\bar{\varepsilon}) \qquad \text{in} \quad \Omega_{\mathrm{s}}, \tag{38}$$

$$\sigma_{\mathrm{s}} = \boldsymbol{C} : \varepsilon \quad \text{in} \quad \Omega_{\mathrm{s}}, \tag{39}$$

$$(-\omega^2 \mathbf{M}_{\mathrm{f}} + \mathbf{K}_{\mathrm{f}}) \cdot \tilde{\mathbf{a}}_{\mathrm{f}} = \mathbf{f}_{\mathrm{f}}(\bar{\varepsilon}) \qquad \text{in} \quad \Omega_{\mathrm{f}}, \tag{40}$$

$$\sigma_{\mathrm{f}} = c^2 \rho_{\mathrm{f}} \nabla \cdot \mathbf{u}\, \mathbf{I} + 2i\omega\eta\, \varepsilon + i\omega\xi\, \nabla \cdot \mathbf{u}\, \mathbf{I} \quad \text{in} \quad \Omega_{\mathrm{f}}, \tag{41}$$

$$[\tilde{\mathbf{u}}] = \mathbf{0} \quad \text{on} \quad \Gamma = \Omega_{\mathrm{s}} \cup \Omega_{\mathrm{f}}, \tag{42}$$

$$\tilde{\mathbf{u}}^{+} = \tilde{\mathbf{u}}^{-} \quad \text{on} \quad \partial\Omega. \tag{43}$$

Here again the indices s and f are used for different phases. In the equations of motion (38) and (40) the volume forces are neglected but the influence of macrodeformation is introduced. On opposite faces of the RVE, microfluctuations must be periodic due to the Hill-Mandel macrohomogeneity condition (43). As defined in Chap. 3.1, equations (39), (41) are constitutive laws and (42) is coupling condition.

3.5 Effective elasticity tensor - output from the microscale

The final results of the microscale calculations is the effective elasticity tensor. In the theory of linear hyperelasticity this tensor is defined as the second derivative of the potential functional $\overline{\psi}(\overline{\varepsilon})$ with respect to the infinitesimal strain tensor or equivalently, the first derivative of the Cauchy stress tensor with respect to the same tensor

$$\overline{\boldsymbol{C}} = \frac{\partial^2 \overline{\psi}(\overline{\varepsilon})}{\partial \overline{\varepsilon}^2} = \frac{\partial \overline{\sigma}}{\partial \overline{\varepsilon}}. \tag{44}$$

In our case, due to the heterogeneity of the material, an analytic expression for the stress is not available so that the numerical interpretation of (44) is necessary. Bearing in mind the vector notation for stresses and strains typical for FEM

$$\overline{\sigma} = \{(\overline{\sigma}^{\mathrm{R}})^{\mathrm{T}} \quad i(\overline{\sigma}^{\mathrm{I}})^{\mathrm{T}}\}^{\mathrm{T}},$$

$$(\overline{\sigma}^{\mathrm{R}})^{\mathrm{T}} = \{\overline{\sigma}^{\mathrm{R}}_{11} \quad \overline{\sigma}^{\mathrm{R}}_{22} \quad \overline{\sigma}^{\mathrm{R}}_{33} \quad \overline{\sigma}^{\mathrm{R}}_{12} \quad \overline{\sigma}^{\mathrm{R}}_{23} \quad \overline{\sigma}^{\mathrm{R}}_{13}\},$$
$$(\overline{\sigma}^{\mathrm{I}})^{\mathrm{T}} = \{\overline{\sigma}^{\mathrm{I}}_{11} \quad \overline{\sigma}^{\mathrm{I}}_{22} \quad \overline{\sigma}^{\mathrm{I}}_{33} \quad \overline{\sigma}^{\mathrm{I}}_{12} \quad \overline{\sigma}^{\mathrm{I}}_{23} \quad \overline{\sigma}^{\mathrm{I}}_{13}\}$$

$$\overline{\varepsilon} = \{(\overline{\varepsilon}^{\mathrm{R}})^{\mathrm{T}} \quad i(\overline{\varepsilon}^{\mathrm{I}})^{\mathrm{T}}\}^{\mathrm{T}},$$

$$(\overline{\varepsilon}^{\mathrm{R}})^{\mathrm{T}} = \{\overline{\varepsilon}^{\mathrm{R}}_{11} \quad \overline{\varepsilon}^{\mathrm{R}}_{22} \quad \overline{\varepsilon}^{\mathrm{R}}_{33} \quad 2\overline{\varepsilon}^{\mathrm{R}}_{12} \quad 2\overline{\varepsilon}^{\mathrm{R}}_{23} \quad 2\overline{\varepsilon}^{\mathrm{R}}_{13}\}$$
$$(\overline{\varepsilon}^{\mathrm{I}})^{\mathrm{T}} = \{\overline{\varepsilon}^{\mathrm{I}}_{11} \quad \overline{\varepsilon}^{\mathrm{I}}_{22} \quad \overline{\varepsilon}^{\mathrm{I}}_{33} \quad 2\overline{\varepsilon}^{\mathrm{I}}_{12} \quad 2\overline{\varepsilon}^{\mathrm{I}}_{23} \quad 2\overline{\varepsilon}^{\mathrm{I}}_{13}\}$$

the numerical interpretation of (44) can be written as

$$\overline{C}_{ij} \approx \frac{1}{\varepsilon}[\overline{\sigma}_i(\overline{\varepsilon}^{\,\varepsilon j}) - \overline{\sigma}_i(\overline{\varepsilon})] \tag{45}$$

where $\overline{\varepsilon}^{\,\varepsilon j}$ is the perturbated strain tensor so that $\overline{\varepsilon}_i^{\,\varepsilon j} = \overline{\varepsilon}_i$ for $i \neq j$ and $\overline{\varepsilon}_i^{\,\varepsilon j} = \overline{\varepsilon}_i + \varepsilon$ for $i = j$. The indices i and j relate to the vector (and not to the tensor notation) for the strains ε: $i, j = 1, \ldots 12$. ε represents a small perturbation. The whole elasticity tensor $\overline{\boldsymbol{C}}$ is now of the dimension 12x12 and it consists of two real and two imaginary submatrices (form analogous to (27)).

Repeating calculations based on (45) for different geometries of the RVE, it is possible to study the change of material strength caused by the process of osteoporosis. Three groups of tests can be performed as three parameters determine the RVE geometry defined in Chap. 3.1 (Fig. 2). In each of the groups one of the geometry parameters is varied while the other ones are kept constant. The diagrams in Fig. 3 show the change of two terms of the elasticity tensors, C_{11} and C_{12}, with respect to the porosity. The increasing porosity is simulated by changing the wall width b in the range from 0.2 to 0.125 mm, whereby the thickness of the solid wall d amounts to 0.1 mm as a first case and 0.05 mm as a second one. Side length a is 1 mm in both cases. Except the parameters given in Table 1 the remaining values used are logarithmic decrement corresponding to the sound motion through the bone $\delta = 0.1$, viscosity coefficient $\xi = 0$, and

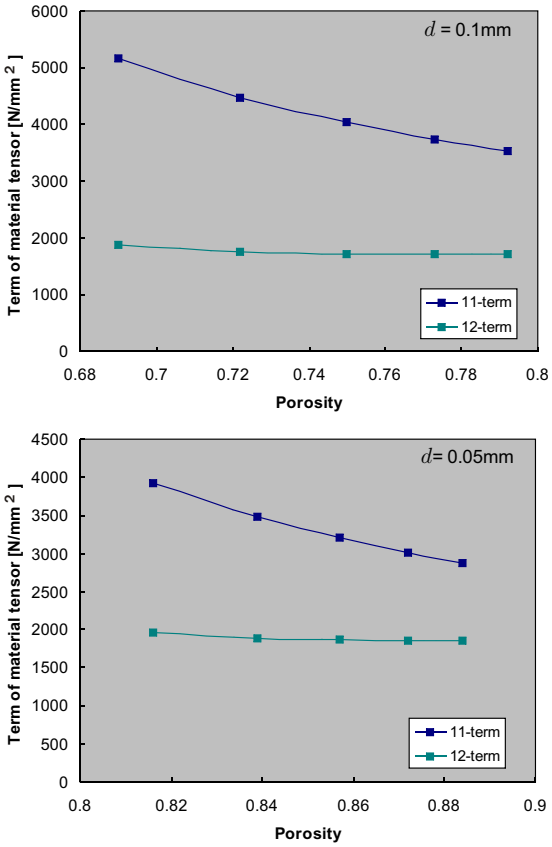

Fig. 3 Change in the real components C_{11} and C_{12} of the elasticity tensor with increasing porosity. The solid wall thickness d takes the values 0.1 and 0.05 mm.

excitation frequency 100 kHz. The change of terms C_{17} and C_{18} belonging to the imaginary part are shown in Fig. 4.

Since experimental investigations have shown that the disappearing of the complete solid walls has the strongest influence on the decrease in material strength, such a process was simulated, too. According to the results presented in the work of McKelvie and Palmer (1991), osteoporosis causes an increase of the spacings of the solid walls from 0.471 to 2.2 mm which is simulated by increasing the side length of the cube-shaped RVE, thereby the wall thickness is kept at d=0.05 mm and wall width at $b = a/6$. The results are presented in Fig. 5 where the abscissas are side length and porosity respectively. The latter diagram shows that with increasing porosity both terms of the elasticity tensor tend to the value 2000 N/mm^2, which corresponds to the limiting case of pure marrow.

3.6 Effective material parameters

The calculated effective elasticity tensors further permit the evaluation of the effective material parameters, which will

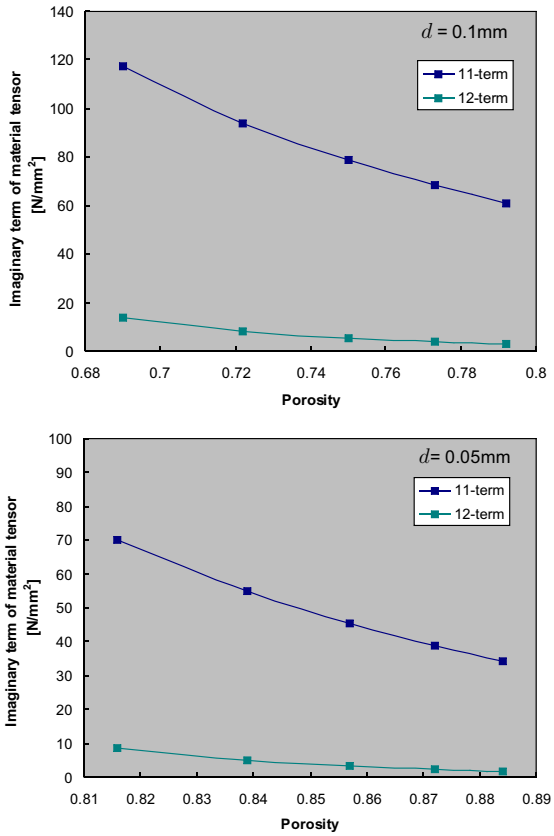

Fig. 4 Change in the imaginary components of the elasticity tensor C_{71} and C_{81} with increasing porosity for different thicknesses of the solid wall d.

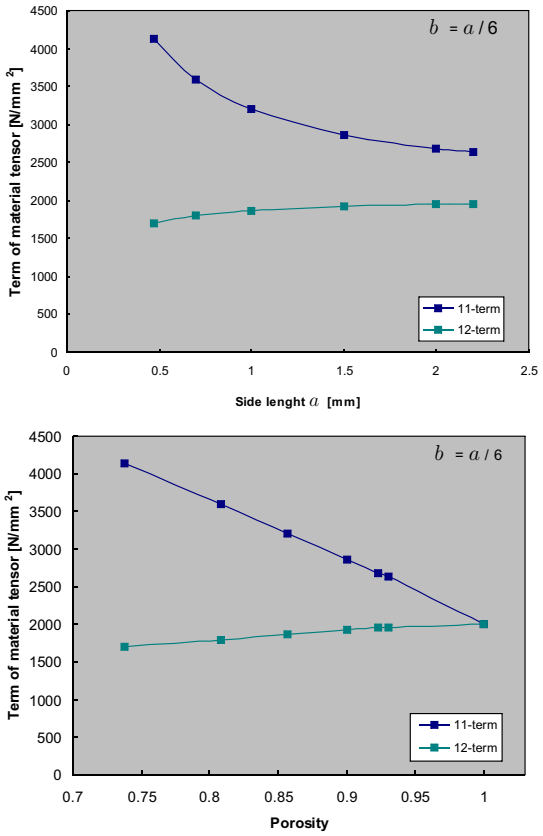

Fig. 5 Change in components C_{11} and C_{12} with increasing spans a and corresponding porosity. Width of solid wall $b = a/6$.

be presented in the following example. For the RVE determined by the parameters a=1 mm, d=0.05 mm, b=0.25 mm (Fig. 2), the real part of the elasticity tensor is given by (46) and it corresponds to the cubic material symmetry in which case the compliance tensor has a form shown in (47) with the shear modulus G. Obviously, calculating the inverse matrix of (46), the material parameters can be directly evaluated.

$$\boldsymbol{C}^{\mathrm{R}} = \begin{bmatrix} 3927.9 & 1959.5 & 1959.5 & 0 & 0 & 0 \\ 1959.5 & 3927.9 & 1959.5 & 0 & 0 & 0 \\ 1959.5 & 1959.5 & 3927.9 & 0 & 0 & 0 \\ 0 & 0 & 0 & 272.9 & 0 & 0 \\ 0 & 0 & 0 & 0 & 272.9 & 0 \\ 0 & 0 & 0 & 0 & 0 & 272.9 \end{bmatrix} \left[\frac{\mathrm{N}}{\mathrm{mm}^2}\right] \tag{46}$$

$$\mathbf{S} = \begin{bmatrix} 1/E & -\nu/E & -\nu/E & 0 & 0 & 0 \\ -\nu/E & 1/E & -\nu/E & 0 & 0 & 0 \\ -\nu/E & -\nu/E & 1/E & 0 & 0 & 0 \\ 0 & 0 & 0 & 1/G & 0 & 0 \\ 0 & 0 & 0 & 0 & 1/G & 0 \\ 0 & 0 & 0 & 0 & 0 & 1/G \end{bmatrix} \tag{47}$$

A further topic of interest is to follow the influence of osteoporosis on effective material behavior. To this end, the effective material parameters are calculated for the effective elasticity tensors explained in the previous section (3.5). In Fig. 6, the results corresponding to the RVEs with wall width b in the interval 0.125-0.25 mm and wall thickness d=0.1 mm and d=0.05 mm are considered. The side length a=1 mm is kept constant. Dependence of Young's modulus and shear modulus on porosity is a smooth, monotonically decreasing function while Poisson's ratio shows opposite behavior: it increases with increasing porosity. Young's modulus takes the values in the interval 1417.17-4163.74 N/mm^2, the shear modulus 32.55-477.82 N/mm^2 and Poisson's ratio 0.266-0.392 for the density 1067-1263 kg/m^3.

3.7 Analysis of the dry skeleton

As the standard literature (Ashman et al, 1984, 1987; Ashman and Rho, 1988; Hoffler et al, 2000; Rho et al, 1993; Williams and Johnson, 1989; Zysset et al, 1999; Zysset, 2003) mostly investigates the effective elasticity parameters of the pure solid phase, for the purpose of comparison, the calculations described in Chap. 3.4 are repeated for the RVE without marrow core (Fig. 2). In this case, in the system (38)-(43), equations related to the solid phase and Hill macrohomogeneity condition stay active while the equations related to the liquid phase and coupling condition have to be left

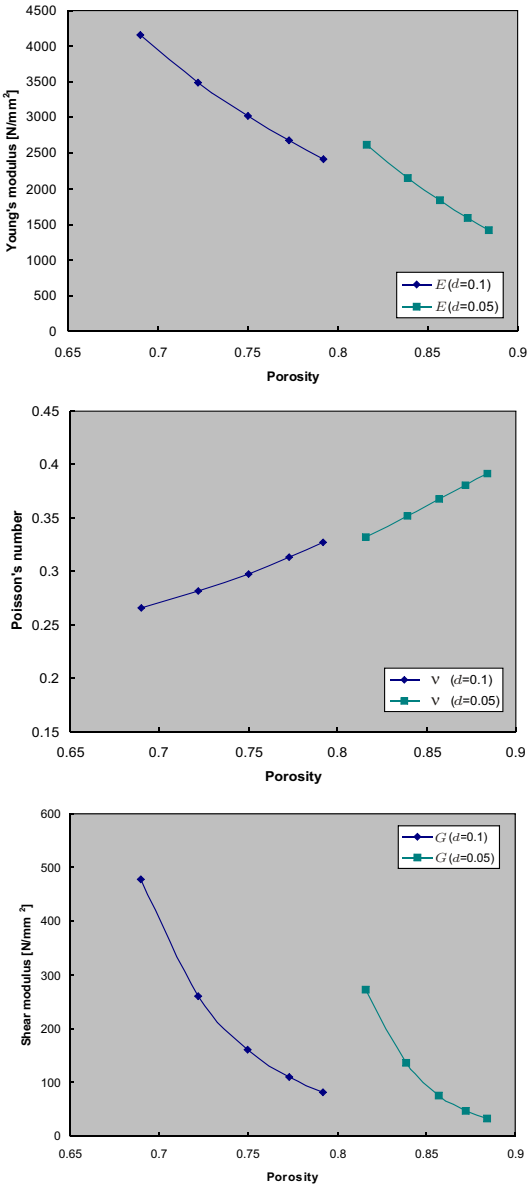

Fig. 6 Change in the real part of effective material parameters versus porosity for the biphasic material.

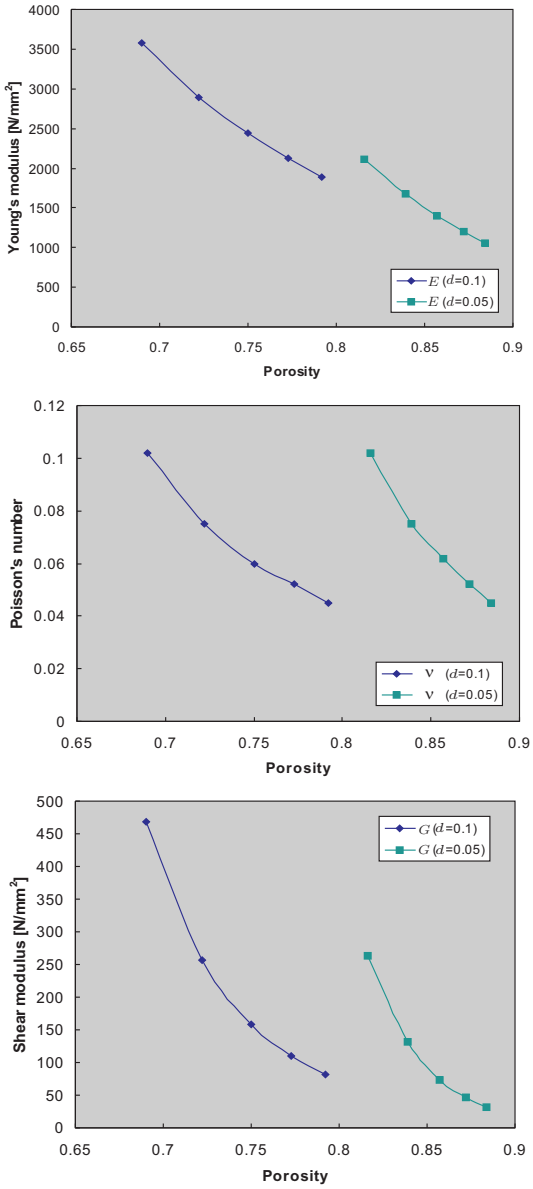

Fig. 7 Change in effective material parameters over porosity for the dry skeleton.

out. The final results at the microlevel are again effective elasticity tensors and material parameters.

Figure 7 shows that in the case of wall thickness of 0.1 mm, the effective Young's modulus takes the values 1883.44-3576.42 N/mm^2 while for a wall thickness of 0.05 mm, the values are between 1050.60 and 2114.80 N/mm^2. These results agree well with the results obtained by Ashman and Rho (1988), who found using ultrasonic tests, that the structural elasticity modulus of cancellous bone has the values in the interval 985-2110 N/mm^2.

The shear modulus takes values in the range 81.17-468.97 N/mm^2 in the first case (d=0.1 mm) and 31.93-263.34 N/mm^2 in the second case (d=0.05 mm). A comparison with the results obtained by an analysis of the biphasic material (Fig.6) shows that the presence of the liquid phase does not significantly influence the values of this material parameter. This of course can be justified by the fact that the shear resistance of the fluid can be neglected. The situation in the case of Poisson's ratio is quite opposite. This parameter takes values in the range 0.045-0.102 for the dry skeleton. The values are falling with increasing porosity while for the biphasic material they are increasing. The great influence of marrow on Poisson's ratio can be explained by the nearly incompressible nature of this material.

4 Macroscale: Simulation of the ultrasonic test

4.1 Ultrasonic attenuation test

While the previous discussion concentrates on the modeling of the RVE as well as on the calculation of the effective material parameters, the main topic of the following part will be the application of the method developed to the simulation of the behavior of the whole bone or of its parts. This task belongs to the domain of macroscale calculations and a simulation of the ultrasonic attenuation test is chosen for an illustration.

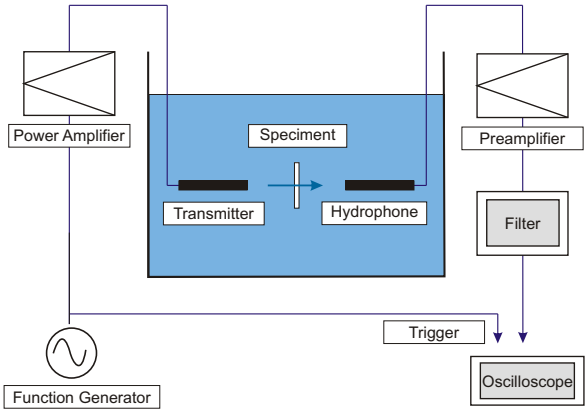

Fig. 8 Laboratory test of Hosokawa and Otani (1997).

The set-up of such a test carried out by Hosokawa and Otani (1997) is shown in Fig. 8. Here a transmitter and hydrophone are submerged in distilled water at $23 \pm 0.5^{\circ}$C and the bone specimen is placed between them. The chosen frequency bandwidth of excitation waves is 0.5-5 MHz. The test uses samples measuring 20-30 mm, with two different thicknesses d_1=9 mm and d_2=7 mm. The samples are chosen to represent the different types of cancellous bone whose densities vary in the range of 1120 - 1200 kg/m^3. Before proceeding to the experiments, the samples are saturated with water in order to remove air bubbles formed in the process of preparation. Using such a test, wave speed v and attenuation α can be calculated according to the standard expressions (Hosokawa and Otani, 1997):

$$v = \frac{\Delta d\, v_0}{\Delta d - (\Delta\phi/\omega) v_0} (=) \frac{\text{mm}}{\text{s}}, \tag{48}$$

$$\alpha = \frac{\ln \Delta V}{\Delta d} (=) \frac{\text{Np}}{\text{mm}} \tag{49}$$

where Δd represents the difference in thickness $\Delta d = d_1 - d_2$, v_0 is the propagation speed in water, $\Delta\phi$ is the phase difference, ω the frequency of initial signals and ΔV is the ratio of amplitude spectra for two different thickness $\Delta V = \frac{V2}{V1}$.

4.2 FEM model of the ultrasonic test

In the FE modeling of the described test, we start from the fact the applied sound excitation is given by a harmonic function in time $\bar{\mathbf{p}}(\mathbf{x},t) = \bar{\mathbf{p}}(\mathbf{x})e^{i\omega t}$, causing periodic displacements $\bar{\mathbf{u}}(\mathbf{x},t) = \bar{\mathbf{u}}(\mathbf{x})e^{i\omega t}$. The problem which has to be solved is than summarized as it follows:

$$-\omega^2 \bar{\rho}\, \bar{\mathbf{u}}(\mathbf{x}) - \bar{\nabla}\cdot\bar{\sigma}(\mathbf{x}) = \mathbf{0}, \tag{50}$$

$$\bar{\sigma}(\mathbf{x}) = \bar{\boldsymbol{C}} : \bar{\varepsilon}(\mathbf{x}), \tag{51}$$

$$\bar{\mathbf{u}}(\mathbf{x}) = \bar{\mathbf{u}}^*(\mathbf{x}) \quad \text{on} \quad \partial\bar{\mathscr{B}}_u, \tag{52}$$

$$\bar{\sigma}(\mathbf{x}) \cdot \bar{\mathbf{n}}(\mathbf{x}) = \bar{\mathbf{p}}(\mathbf{x}) \quad \text{on} \quad \partial\bar{\mathscr{B}}_p. \tag{53}$$

Here in the equation of motion (50) volume forces are neglected, and the only external load is due to the sound pressure acting on the boundary part $\partial\bar{\mathscr{B}}_p$, $\bar{\mathbf{u}}^*(\mathbf{x})$ are displacements given on the Dirichlet boundary part $\partial\bar{\mathscr{B}}_u$. The constitutive law (51) depends on the effective elasticity tensor $\bar{\boldsymbol{C}}$ obtained from the microscale. As stated at the beginning, the overbar denotes quantities related to the macrolevel.

Concerning the geometrical properties of the FE model, the following remarks are necessary. First, as the water in the original test is used only as a transmitter whose attenuation can be neglected, in the FE model, consideration has to be given only to the behavior of the sample. Second, as the sound wave is longitudinal, the whole simulation may be considered as a 2D problem of wave propagation through the thin slice of the sample (Fig. 9). Moreover, the displacements in x_2 direction at all points have to be suppressed, while the results will show that displacements in x_3 direction are of an order smaller than those in x_1 direction, which fits in with the nature of sound waves.

The dimension of the sample transversal to the direction of wave propagation is assumed to be 50 mm, which in any case is greater than the wavelength of the excitation sound waves (see Chap. 4.3). Two kinds of boundary conditions are simulated at the top and the bottom of the specimen. In the first case, it is presumed that all displacements at all points on these two boundaries are constrained. In the second case, only the middle points on the top and bottom boundary are supported. The results show that the type of boundary conditions on these two boundaries does not influence the results.

The size of the specimen in the direction of wave propagation is chosen as 30 mm. The discretization of the sample and applied load are shown in Fig. 9. Here the number of elements is 100x50. The thickness in the direction ”2” is 0.5 mm. The sound pressure p=8 kPa acts on the left boundary of the sample. The diameter of the pulser is assumed to be 10 mm. The last few parameters (thickness of the specimen, pressure and diameter of the transmitter) are chosen arbitrarily as they do not have any significant influence on the simulation.

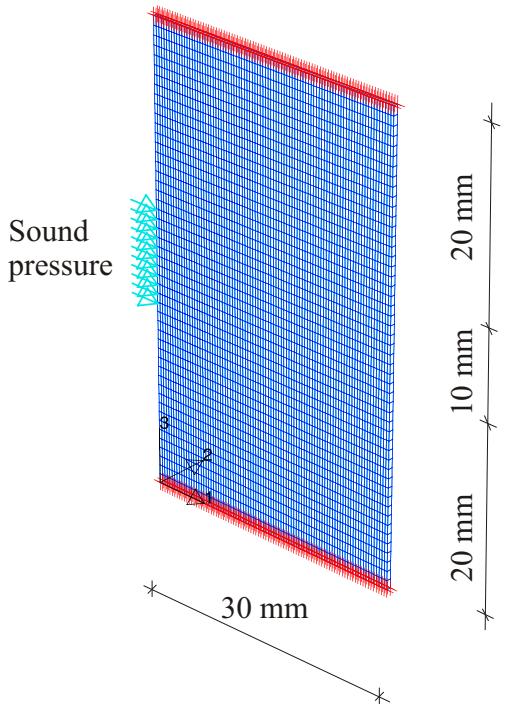

Fig. 9 Model for FEM simulation of wave propagation through cancellous bone.

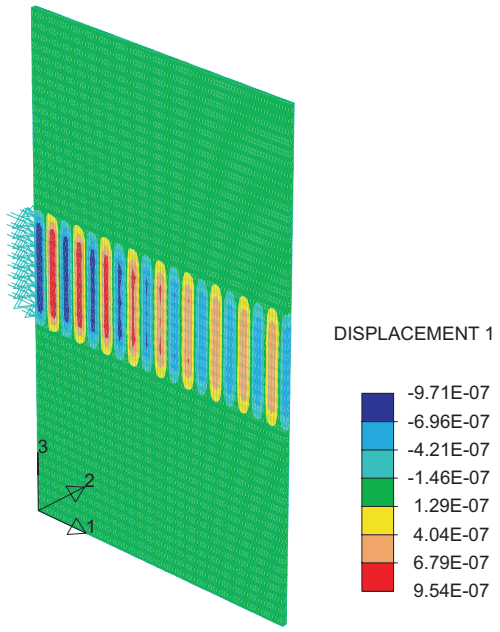

Fig. 10 Wave propagation through cancellous bone with an RVE geometry determined by the parameters a=1 mm, d=0.1 mm, b=0.25 mm. Assumed excitation frequency 0.6MHz.

4.3 Test example

The velocity of wave propagation through the solid bodies is dependent on the material properties but also on the shape of the body and especially on its dimensions. In particular there are two kinds of sound velocity to be distinguished: the wave velocity through the bounded medium, also known as the bar velocity (c_b) and the velocity through the unbounded medium (c_u). Here, the term "bounded" means that cross-sectional dimensions of the sample, transverse to the direction of wave motion, have to be smaller than the wavelength. The mentioned velocities are defined by the following expressions (Ashman and Rho, 1988; Marsden and Hughes, 1983)

$$c_b = \sqrt{\frac{E}{\rho}}, \tag{54}$$

$$c_u = \sqrt{\frac{\lambda + 2\mu}{\rho}}. \tag{55}$$

where λ and μ are the Lamé parameters. Observation is that the velocity in unbounded medium becomes greater than in the bounded one. In scope of biomechanics, equation (55) appears often in the form $C_{11} = \rho c_u^2$ whereby C_{11} represents the 11-component of the elasticity tensor (Williams and Johnson, 1989).

Using the results from Chap. 3.6 and the expressions (54) and (55) the wave velocities through the cancellous bone can be calculated and used as a check of the FEM simulations. This is illustrated by an example where consideration is given to the wave propagation through the homogenized bone with an RVE geometry determined by the parameters a=1 mm, d=0.1 mm and b=0.25 mm. The model shown in Fig. 9 corresponds to the case of an unbounded medium, so that the expected wave velocity amounts to c_u = 2021.69 m/s. For an arbitrarily chosen excitation frequency f=0.6 MHz, the expected wavelength is 3.37 mm. The results of the FEM simulation shown in Fig. 10 endorse such expectations as the resulting wavelength λ is approximately 3.24 mm (9.25 wavelengths on the length of sample which amounts to 30 mm). The wavelength is connected to velocity c and frequency f by the relation $\lambda = c/f$. An additional check looks at the amplitude of particle oscillations u related to wave pressure p by using expression

$$u = \frac{p}{2\pi f c \rho}. \tag{56}$$

This relation can be derived using the definition of the wave impedance and belongs to the basics of acoustic theory (Hall, 1993). By using (56), it can be shown that the approximate particle amplitude for the example discussed in this section has the value $8.32 \cdot 10^{-7}$mm, which agrees with the displacement values shown in Fig. 10 where the mean value of the slightly attenuated amplitudes amounts to $8.335 \cdot 10^{-7}$mm.

4.4 Wave attenuation

The last group of simulations considers the analysis of wave attenuation. Here the propagation of waves of different frequencies through samples with different material parameters is simulated in order to check the experimentally obtained result that increasing excitation frequency and material density cause increasing attenuation.

Firstly, consideration is given to the influence of increasing excitation frequency on bone behavior. To this end the type of material microstructure in the simulations is fixed, and sound excitation at different frequencies is applied.

As the influence of attenuation is more noticeable in the case of higher frequencies, excitation is simulated in the domain 0.9-1.7 MHz. The microstructure is chosen according to the geometry of the RVE (Fig. 2) determined by the parameters a=1 mm, b=0.25 mm and d=0.05 mm (ρ=1136 kg/m^3). The results of the simulations are shown in Fig. 11 where the stronger attenuation obviously corresponds to higher frequencies.

The study of the relationship between attenuation and density is more complicated than of the influence of excitation frequency. This can be expected, because the RVE geometry presented in Chap. 3.1 is determined by three parameters (wall thickness d, wall width b and side length a). Correspondingly, three different types of tests can be carried out. In each group of tests, two of the geometrical parameters have to be kept constant and the remaining one is varied. For illustration, the results obtained by changing the wall width are shown in Fig. 12. The results are obtained by investigating materials with RVE such that a=1 mm, d=0.05 mm and the width of wall b takes the values 0.25-0.125 mm. Figure 12 shows that decreasing density causes decreasing attenuation. Similar results are obtained for the decreasing density caused by the decreasing wall thickness or increasing side length (Ilic, 2008).

From Figs. 11 and 12, the conclusion can be drawn that the numerical simulations endorse experimental results: the greater excitation frequency and sample density correspond to the greater attenuation. The numerical values attenuation are obtained by using expression

$$\alpha = \frac{\ln \Delta V'}{\Delta d'} \tag{57}$$

where, in the contrast to (49), $\Delta V'$ represents the ratio of the amplitudes at two points of the same sample, laying at the same horizontal level, but with the distance $\Delta d'$ amounting to the integer number of the wave lengths. The obtained values amount on average to 0.115-0.225 Np/cm, which is approximately the same as if they would be obtained by superposition of the attenuation due to the solid frame and fluid core separately. However the values are smaller than those obtained experimentally. This can be explained by the missing traction term at the phase interface which is at the same time, an idea for a possible improvement of the model in the future work.

The final question to be considered here is the distinction of the fast and the slow wave. The existence of these two kinds of waves was predicted by Biot (Biot, 1956a,b) and experimentally observed by Hosokawa and Otani (1997). But the question if and when these two waves appear still is an open issue and in some experimental studies only a single wave is observed (Nicholson et al, 1996; Strelitzki and Evans, 1996; Droin et al, 1998; Wear, 2000). In their work Hosokawa and Otani (1998) show that the appearance of a second wave is dependent on the inclination of the incident wave to the trabeculae alignment. If the wave propagates perpendicularly to the direction of the trabeculae, the slow and the fast wave overlap completely in time and the second wave cannot be observed. In the case that the propagation direction of the wave coincides with the longitudinal direction of trabeculae, the second wave will appear. Another approach document the existence of mixed-modes were both waves overlap in time (Bauer et al, 2008; Anderson et al, 2008; Padilla and Laugier, 2000; Hughes et al, 1999). The results presented in this chapter show that at the current stage the homogenization technique allows simulation solely of a single longitudinal wave which can be regarded as mixed-mode wave. The reason for this shortcoming could be the fact that our model still does not include the scattering effects which may be an important factor influencing the separation of waves as well as the high attenuation (Padilla et al, 2008; Bas et al, 2004; Luppé et al, 2002; Haïat et al, 2008b,a).

5 Conclusions

This contribution is concerned with the multiscale modeling of cancellous bone. The assumed RVE consisting of thin walls and the marrow core is described and the process of osteoporosis is simulated by varying the geometrical parameters. The results in this phase show that Young's and shear modulus decrease monotonically and Poisson's ratio increases monotonically with increasing porosity. For the tests with the constant unit side length of the RVE, the values of Young's modulus are in the interval 1417.17-4163.74 N/mm^2 and of the shear modulus 32.55-477.82 N/mm^2. Poisson's ratio amounts to 0.266-0.392. The calculations are repeated also for the pure skeleton, and these results are compared with those experimentally obtained, showing an excellent agreement. The Young's modulus in this case amounts to 1050.60-2114.80 N/mm^2 for d=0.05 mm. A further comparison with results obtained when considering cancellous bone as a biphasic material shows that the marrow phase has a great influence on Poisson's ratio and a small influence on the shear modulus, which is justified by the small shear resistance and the high Poisson's ratio of the fluid phase.

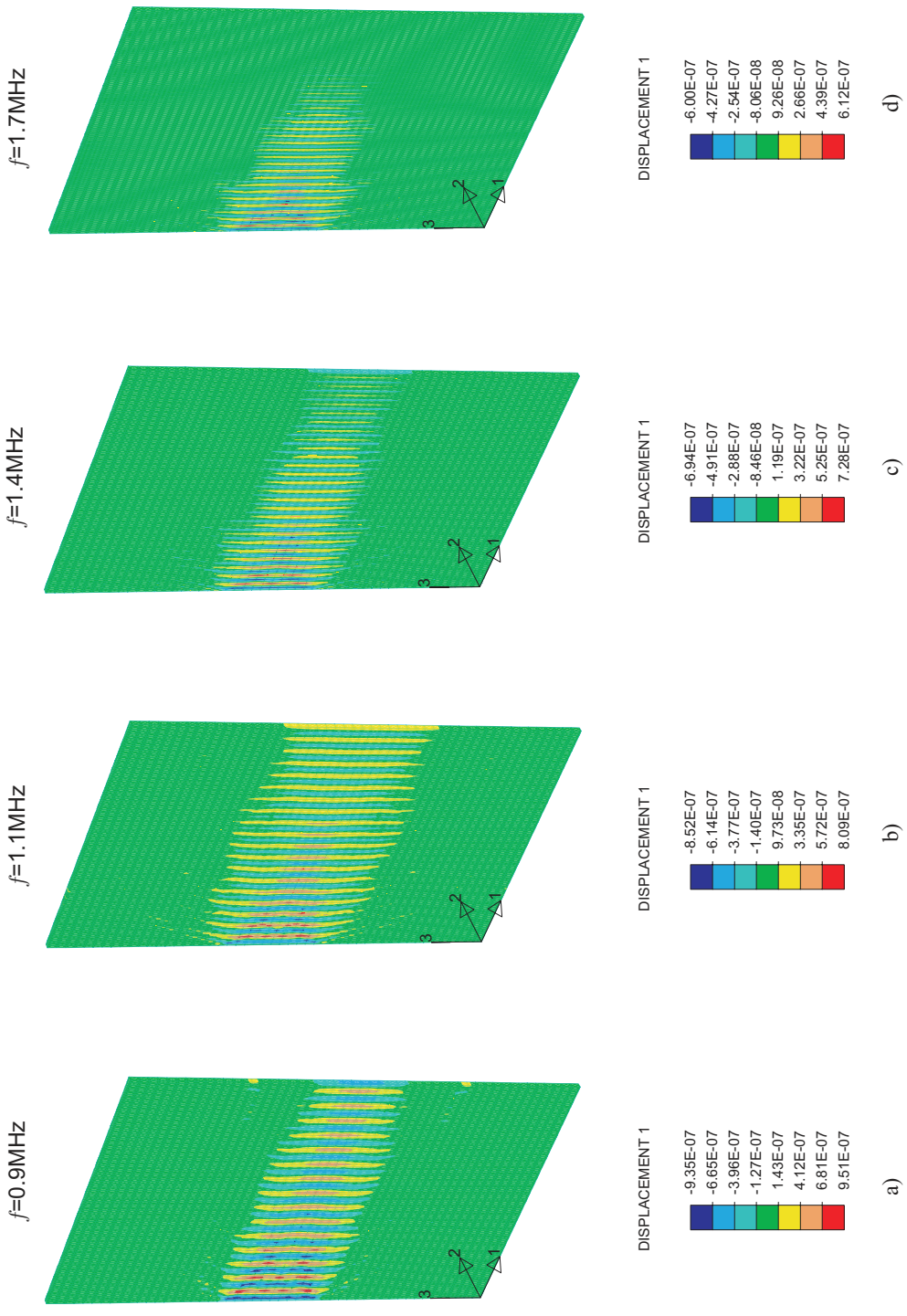

Fig. 11 Wave propagation of sound waves of different frequencies through the bone whose geometry of RVE is determined by the parameters a=1 mm, b=0.25 mm and d=0.05 mm.

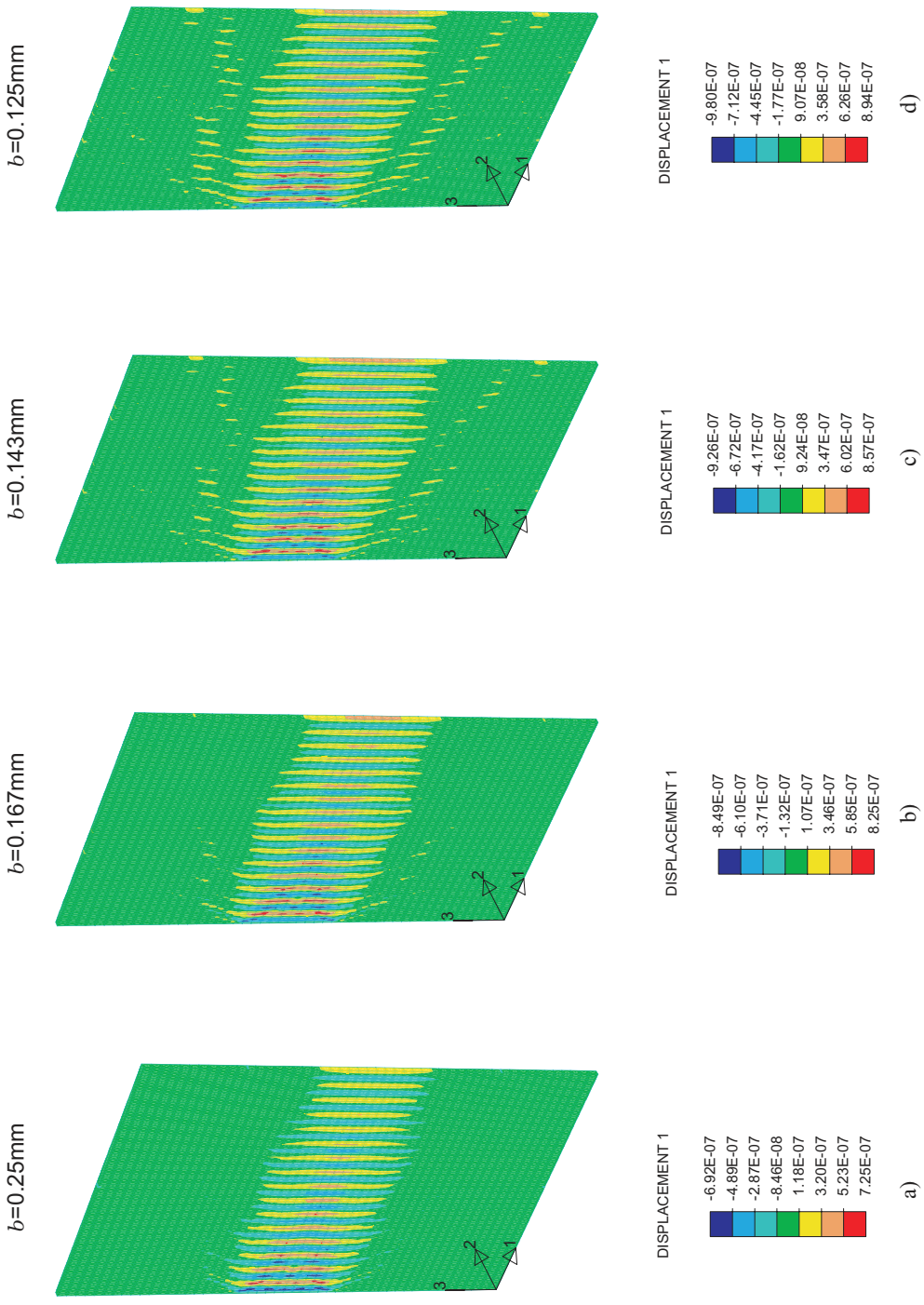

Fig. 12 Wave propagation of the wave of frequency 1MHz in the case that material microstructure is determined by the parameters a=1 mm and d=0.05 mm. The width of the solid wall is changeable taking the values 0.25, 0.1667, 0.143 and 0.125 mm.

The later part of the paper concentrates on macroscale calculations and particularly on the simulation of the ultrasonic attenuation test. To this end the wave propagation through the two-dimensional FE model of the sample is simulated. In the different tests, the excitation frequency as well as the geometrical properties of the RVE are varied. The results obtained in this phase endorse the experimental findings that increasing density and excitation frequency cause an increasing attenuation coefficient, but the numerical values show deviation from values obtained experimentally. This, of course, provides a motivation for further improvement of the RVE and an idea is to change the coupling condition on the phase interface and to introduce the contact friction. As the solid frame has a great specific surface, this contribution may have an important influence. Furthermore, an implementation of scattering effects and alternative constitutive laws for the phases could also lead to more realistic values for the attenuation coefficient.

Although an improvement of the RVE is contemplated, the results have shown that the multiscale FEM is a method very convenient to study this type of material. Some of its useful properties are the short calculation time and the wide spectrum of application regarding micro- and macroscopic problems. Moreover the simulations at the microlevel allow the comparison with experimental results and thus a reliable analysis yielding optimal geometrical parameters. Because of this, the method is also a good starting point for solving inverse problems.

References

Anderson CC, Marutyan KR, Holland M, Wear KA, Miller JG (2008) Interference between wave modes may contribute to the negative dispersion observed in cancellous bone. J Acoust Soc Am 124(3):1781–1789

Ashman RB, Rho JY (1988) Elastic modulus of trabecular bone material. J Biomechanics 21(3):979–986

Ashman RB, Corin JD, Buskirk WCV, Rice JC (1984) A continuous wave technique for the measurement of the elastic properties of cortical bone. J Biomechanics 17(5):349–361

Ashman RB, Corin JD, Turner CH (1987) Elastic properties of cancellous bone: measurement by an ultrasonic technique. J Biomechanics 20(10):979–986

Barkmann E, Kantorovich E, Singal C, Hans D, Genant H, Heller M, Gluer C (2000a) A new method for quantitative ultrasound measurement at multiple skeletal sites. J Clin Densitometry 3:1–7

Bas PYL, Luppé F, Conoir JM, Franklin H (2004) N-shell cluster in watter: multiple scattering and splitting of resonances. J Acoust Soc Am 115(4):1460–1467

Bathe KJ (1996) Finite element procedures. Prentice-Hall International

Batoz JL, Tahar MB (1982) Evaluation of new quadrilateral thin plate bending element. Int J Num Meth Eng 18:1655–1677

Bauer AQ, Marutyan KR, Holland MR, Miller JG (2008) Negative dispersion in bone: The role of interference in measurements of the apparent phase velocity of two temporally overlapping signals. J Acoust Soc Am 123(4):2407–2414

Bayraktar HH, Morgan EF, Niebur GL, Morris GE, Wong EK, Keaveny TM (2004) Comparison of the elastic and yield properties of human femoral trabecular and cortical bone tissue. J Biomechanics 37(1):27–35

Biot MA (1956a) Theory of propagation of elastic waves in fluid-saturated porous solid. I. Low-frequency range. Jour Acoust Soc Am 28(2):168–178

Biot MA (1956b) Theory of propagation of elastic waves in fluid-saturated porous solid. II. Higher frequency range. Jour Acoust Soc Am 28(2):179–191

Bossy E, Talmant M, Laugier P (2004) Three-dimensional simulations of ultrasonic axial transmission velocity measurement on cortical bone models. J Acoust Soc Am 115:2314–2324

Bossy E, Talmant M, Laugier P (2004a) Bi-directional axial transmission can improve accuracy and precision of ultrasonic velocity measurement in cortical bone: a validation on test material. IEEE TransUltrason Ferroelectr Freq Control 51:71–79

Bossy E, Padilla F, Peyrin F, Laugier P (2005) Three-dimensional simulation of ultrasound propagation through trabecular bone structures measured by synchrotron microtomography. Phys Med Biol 50:5545–5556

Buchanan JL, Gilbert RP (2006) Determination of the parameters of cancellous bone using high frequency acoustic measurements. Math Computer Model 45(3-4):281–308

Buchanan JL, Gilbert RP, Khashanah K (2002) Recovery of the poroelastic parameters of cancellous bone using low frequency acoustic interrogation. In: Wirgin A (ed) Acoustic, Mechanics, and the related Topics of mathematical Analysis, World Scientific:, pp 41–47

Buchanan JL, Gilbert RP, Khashanah K (2004) Determination of the parameters of cancellous bone using low frequency acoustic measurements. J Comput Acoust 12(2):99–126

Droin P, Berger G, Laugier P (1998) Velocity dispersion of acoustic waves in cancellous bone. IEEE Trans Ultrason Ferroelectr Freq Control 45:581–592

Fang M, Gilbert RP, Panachenko A, Vasilic A (2007) Homogenizing the time harmonic acoustics of bone. Mat Comput Model

Gilbert RP, Lin ZY, Hackl K (1998) Acoustic Green function approximations. J Comput Acoust 6(4):435–452

Hackl K (1997) A framework for nonlinear shells based on generalized stress and strain measures. Int J Solids Struct 34(13):1609–1632

Hackl K (1998) Asymptotic methods in underwater acoustics. In: Florian K, Hackl K, Schnitzer F, Tutschke W (eds) Generalized analytic functions - Theory and Application to Mechanics, Kluwer Academic, pp 229–240

Haïat G, Padilla F, Peyrin F, Laugier P (2007) Variation of ultrasonic parameters with microstructure and material properties of trabecular bone: A three-dimensional model simulation. J Bone Miner Res 22:665–674

Haïat G, Lhémery A, Renaud F, Padilla F, Laugier P, Naili S (2008a) Velocity dispersion in trabecular bone : influence of multiple scattering and of absorption. J Acoust Soc Am 124(6):4047–4058

Haïat G, Padilla F, Peyrin F, Laugier P (2008b) Fast wave ultrasonic propagation in trabecular bone: numerical study of the influence of porosity and structural anisotropy. J Acoust Soc Am 123(3):1694–1705

Hall DE (1993) Basic Acoustics. Krieger Publishing Company, Malabar Florida

Hazanov S, Amieur M (1995) On overall properties of elastic heterogeneous bodies smaller than representative volume. Int J Eng Sci 33(9):1289–1301

Hildebrand T, Rüegsegger P (1997) Qualification of bone microarchitecture with the structure model index. Comp Meth Biomech Biomed Eng 1:15–23

Hill R (1963) Elastic properties of reinforced solids: some theoretical principles. J Mech Phys Solids 11:357–372

Hill R (1972) On constitutive macro-variables for heterogeneous solids at finite strain. Proc R Soc Lond A 326:131–147

Hoffler CE, Moore KE, Kozloff K, Zysset PK, Brown MB, Goldstein SA (2000) Heterogeneity of bone lamellar-level elastic moduli. Bone 26:603–609

Hollister SJ, Kikuchi N (1994) Homogenization theory and digital imaging: a basis for studying the mechanics and design principles of bone tissue. Biotechnol Bioeng 43(7):586–596

Hosokawa A (2006) Ultrasonic pulse waves in cancellous bone analyzed by finite-difference time-domain methods. Ultrasonics 44:227–231

Hosokawa A, Otani T (1997) Ultrasonic wave propagation in bovine cancellous bone. Jour Acoust Soc Am 101:558–562

Hosokawa A, Otani T (1998) Acoustic anisotropy in bovine cancellous bone. J Acoust Soc Am 103:2718–1722

Hughes ER, Leighton TG, Petley GW, White PR (1999) Ultrasonic propagation in cancellous bone: a new stratified model. Ultrasound Med Biol 25:811–821

Ilic S (2008) Application of the multiscale FEM to the modeling of composite materials. Ph.D. Thesis, Ruhr University Bochum, Germany

Ilic S, Hackl K (2004) Homogenisation of random composites via the multiscale finite-element method. PAMM 4:326–327

Ilic S, Hackl K (2007) Application of the multiscale fem to the modeling of heterogeneous materials. Proceedings of the first seminar on The Mechanics of Multifunctional Materials: pp 47–51

Laugier P, Berger G, Giat P, Bonnin-Fayet P, Laval-Jeantet M (1994a) Ultrasound attenuation imaging in the os calcis: an improved method. Ultrason Imaging 16:65–76

Luo G, Kaufman JJ, Chiabrera A, Bianco B, Kinney JH, Haupt D, Ryaby JT, Siffert RS (1999) Computational methods for ultrasonic bone assessment. Ultrasound Med Biol 25:823–830

Luppé F, Conoir JM, Franklin H (2002) Scattering by fluid cylinder in a porous medium: Application to trabecular bone. J Acoust Soc Am 111(6):2573–2582

Marsden JE, Hughes TJR (1983) Mathematical foundations of elasticity. Dover Publications

McKelvie ML, Palmer SB (1991) The interaction of ultrasound with cancellous bone. Phys Med Biol 10:1331–1340

Miehe C, Schotte J, Lambrecht M (2002) Homogenisation of inelastic solid materials at finite strains based on incremental minimization principles. J Mech Phys Solids 50:2123–2167

Mura T (1993) Micromechanics: overall properties of heterogeneous solids. Kluwer Academic Publishers

Nemat-Nasser S, Hori M (1993) Micromechanics: overall properties of heterogeneous materials. Nord-Holland Series in: Applied Mathematics and Mechanics 37

Nicholson PHF, Lowet G, Langton CM, Dequeker J, der Perre GV (1996) A comparison of time-domain and frequency domain approaches to ultrasonic velocity measurement in trabecular bone. Phys Med Biol 41:2421–2435

Niebur GL, Feldstein MJ, Yuen JC, Chen TJ, Keaveny TM (2000) High-resolution finite element models with tissue strength asymmetry accurately predict failure of trabecular bone. J Biomech 33(12):1575–1583

Ostoja-Starzewski M (2006) Material spatial randomness: from statistical to representative volume element. Probab Eng Mech 21(2):112–132

Padilla F, Laugier P (2000) Phase and group velocities of fast and slow compressional waves in trabecular bone. J Acoust Soc Am 108:1949–1952

Padilla F, Jenson F, Bousson V, Peyrin F, Laugier P (2008) Relationship of trabecular bone structure with quantitative ultrasound parameters: In vitro study of human proximal femur using transmission and backscatter measurements. bone 42:1193–1202

Pahr DH, Zysset PK (2008) Influence of boundary conditions on computed apparent elastic properties of cancel-

lous bone. Biomechan Model Mechanobiol 7:463–476
Rho JY, Ashman RB, Turner CH (1993) Young's modulus of trabecular and cortical bone material: Ultrasonic and microtensile measurements. J Biomechanics 26(2):111–119
Rietbergen BV, Odgaard A, Kabel J, Huiskes R (1996) Direct mechanics assessment of elastic symmetries and properties of trabecular bone architecture. J Biomech 29(12):1653–1657
Schröder J (2000) Homogenisierungsmethoden der nichtlinearen Kontinuumsmechanik unter Beachtung von Stabilitäts Problemen. Habilitationsshrift, Universität Stuttgart, Deutschland
Strelitzki R, Evans JA (1996) On the measurement of the velocity of ultrasound in the os calcis using short pulses. Eur J Ultrasound 4:205–213
Taylor RL (1998) Finite element analysis of linear shell problems. In: Whiteman J (ed) The Mathematics of finite element and Applications, VI, Academic Press, London
Torquato S (2002) Random heterogeneous materials: microstructure and macroscopic properties. Springer Verlag, New York
Wanji C, Cheung YK (1997) Refined quadrilateral discrete kirchhoff thin plate bending element. Int J Num Meth Eng 40:3937–3953
Wear KA (2000) Measurement of phase velocity and group velocity in human calcaneus. Ultrasound Med Biol 26:641–646
Williams JL, Johnson WJH (1989) Elastic constants of composites formed from pmma bone cement and anisotropic bovine tibial cancellous bone. J Biomechanics 22(6/7):673–682
Willis JR (1981) Variational and related methods for the overall properties of composites. Adv Appl Mech 21:1–78
Willis JR (1982) Elasticity theory of composites. Mechanics of Solids, the Rodney Hill 60th Anniversary Volume pp 653–686
Zienkiewicz OC, Taylor RL (2000) The finite element method. Butterworth-Heinemann
Zohdi TI, Wriggers P (2005) Introduction to Computational Micromechanics. Springer Series in: Lecture Notes in Applied and Computational Mechanics, 20
Zysset P (2003) A review of morphology-elasticity relationships in human trabecular bone: theories and experiments. J Biomechanics 36:1469–1485
Zysset PK, Guo XE, Hoffler CE, Moore KE, Goldstein SA (1999) Elastic modulus and hardness of cortical and trabecular bone lamellae measured by nanoindentation in the human femur. J Biomechanics 32:1005–1012